Structural changes in the Mn_4Ca cluster and the mechanism of photosynthetic water splitting

Yulia Pushkar*†, Junko Yano*‡, Kenneth Sauer*†, Alain Boussac‡§, and Vittal K. Yachandra*‡

*Physical Biosciences Division, Lawrence Berkeley National Laboratory, Berkeley, CA 94720-8099; †Department of Chemistry, University of California, Berkeley, CA 94720-1460; and §iBiTec-S, Unité de Recherche Associée Centre National de la Recherche Scientifique 2096, Commissariat à l'Energie Atomique Saclay, 91191 Gif sur Yvette, France

Edited by Elisabeth Gantt, University of Maryland, College Park, MD, and approved December 4, 2007 (received for review July 30, 2007)

Photosynthetic water oxidation, where water is oxidized to dioxygen, is a fundamental chemical reaction that sustains the biosphere. This reaction is catalyzed by a Mn_4Ca complex in the photosystem II (PS II) oxygen-evolving complex (OEC): a multiprotein assembly embedded in the thylakoid membranes of green plants, cyanobacteria, and algae. The mechanism of photosynthetic water oxidation by the Mn_4Ca cluster in photosystem II is the subject of much debate, although lacking structural characterization of the catalytic intermediates. Biosynthetically exchanged Ca/Sr-PS II preparations and x-ray spectroscopy, including extended x-ray absorption fine structure (EXAFS), allowed us to monitor Mn–Mn and Ca(Sr)–Mn distances in the four intermediate S states, S_0 through S_3, of the catalytic cycle that couples the one-electron photochemistry occurring at the PS II reaction center with the four-electron water-oxidation chemistry taking place at the $Mn_4Ca(Sr)$ cluster. We have detected significant changes in the structure of the complex, especially in the Mn–Mn and Ca(Sr)–Mn distances, on the S_2-to-S_3 and S_3-to-S_0 transitions. These results implicate the involvement of at least one common bridging oxygen atom between the Mn–Mn and Mn–Ca(Sr) atoms in the O–O bond formation. Because PS II cannot advance beyond the S_2 state in preparations that lack Ca(Sr), these results show that Ca(Sr) is one of the critical components in the mechanism of the enzyme. The results also show that Ca is not just a spectator atom involved in providing a structural framework, but is actively involved in the mechanism of water oxidation and represents a rare example of a catalytically active Ca cofactor.

manganese enzyme | oxygen evolution | photosynthesis | photosystem II | x-ray spectroscopy

Photosynthetic oxidation of water to dioxygen is catalyzed by a Mn_4Ca cluster in the oxygen-evolving complex (OEC) of photosystem II (PS II) (1). PS II is a multiprotein assembly embedded in the thylakoid membranes of green plants, cyanobacteria, and algae. The structure and function of the Mn_4Ca cluster, the heart of the OEC, has been under active investigation by many spectroscopic techniques such as EPR/electron-nuclear double resonance (ENDOR) (2–4), x-ray spectroscopy (5, 6), and FTIR (7, 8). X-ray diffraction (XRD) studies at 3.0–3.8 Å resolution have located the Mn_4Ca cluster in the electron-density map and confirmed the presence of Ca in the cluster (9, 10). Before the XRD studies, the presence of Ca in the OEC was detected by using Ca and Sr x-ray absorption spectroscopy (XAS) studies (11–15). Mn, Ca, and Sr extended x-ray absorption fine structure (EXAFS) studies of PS II frozen solutions have provided accurate distances (≈0.02 Å) and information on the numbers of Mn–Mn, Mn–Ca and Mn/Ca–ligand vectors in the Mn_4Ca cluster (6, 16, 17). XAS experiments require a significantly lower x-ray dose than XRD measurements. The onset of radiation damage can be precisely determined and controlled by monitoring the Mn K-edge position, thus allowing us to collect data from the intact Mn_4Ca cluster of PS II. Recently, a high-resolution Mn_4Ca structural model was determined by using a polarized Mn EXAFS study on PS II single crystals in the S_1 state (18).

Of all the cations that can competitively replace Ca in PS II, only Sr is capable of supporting O_2 evolution, a feature that has been attributed to the similar electronegativities of Ca and Sr and, hence, to their similar Lewis acidities and pK_a values of water ligands (19, 20). Substituting Sr for Ca alters the EPR properties of the S_2 state, increasing the fraction of PS II that exhibits a $g \approx 4.1$ or $g \approx 5.25$ EPR signal and altering the appearance of the $g = 2$ multiline EPR signal (19, 21). The presence of Sr also shifts a low-frequency S_2 state vibrational mode that has been assigned to a Mn–O–Mn structural unit (22) and alters several carboxylate-stretching modes of the $S_2 - S_1$ FTIR difference spectrum (23–26). This demonstrates that Ca substitution for Sr perturbs the structure of Mn_4 cluster only slightly, making Sr a relevant spectroscopic probe.

This x-ray absorption study determines the changes in the Mn–Mn and Ca(Sr)–Mn distances in the four intermediate S states, S_0 through S_3, of the catalytic cycle. This became possible by the use of unique PS II preparations from the thermophilic cyanobacterium, *Thermosynechococcus elongatus*, with Ca biosynthetically replaced by Sr in an isomorphic structure (27). The advantages over Ca/Sr exchange induced by biochemical procedures are: (*i*) an enzyme fully competent in O_2 evolution, (*ii*) a 1:1 Sr-to-PS II ratio monitored by Sr quantitation, and (*iii*) Sr K-edge EXAFS measurements that result in less x-ray damage and are preferred for experimental reasons to those at lower-energy Ca K-edge (13–15).

Results

EPR Spectroscopic Quantitation of S State Composition. Protein samples in the S_1 state were advanced to primarily S_2, S_3, and S_0 states by giving one, two, and three laser flashes followed by immediate freezing in liquid nitrogen (28). Starting from a dark-adapted sample, the S_2 state multiline EPR signal is maximal after one flash and oscillates with a period of four as a function of flash number; thus, the S_2 state multiline EPR signal can be used to characterize the S state distribution of samples given zero, one, two, three, four, five, or six flashes. Supporting information (SI) Fig. 5*A* shows typical EPR spectra obtained after a given flash number. A deep period-four oscillation is observed with maxima on the first and fifth flashes, indicating that there is very little dephasing of S state advancement with flashes and that the initial S state population is close

Author contributions: Y.P., J.Y., K.S., A.B., and V.K.Y. designed research; Y.P., J.Y., A.B., and V.K.Y. performed research; A.B. contributed new reagents/analytic tools; Y.P. analyzed data; and Y.P., J.Y., K.S., A.B., and V.K.Y. wrote the paper.

The authors declare no conflict of interest.

This article is a PNAS Direct Submission.

‡To whom correspondence may be addressed. E-mail: jyano@lbl.gov, alain.boussac@cea.fr, or vkyachandra@lbl.gov.

This article contains supporting information online at www.pnas.org/cgi/content/full/0707092105/DC1.

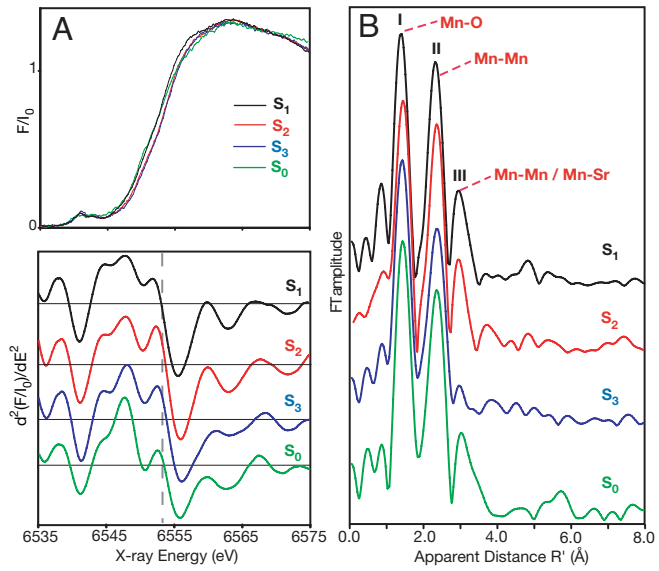

Fig. 1. Mn XAS of Sr-PS II from *T. elongatus*. (*A*) Mn K-edge XANES spectra (*Upper*) and the corresponding second derivatives of the XANES spectra (*Lower*) in the S_1, S_2, S_3, and S_0 states. The inflection point of the edges and the shape of the spectra are clearly different between the S states. (*B*) Fourier transforms of k^3-weighted Mn EXAFS (SI Fig. 6) of Sr-PS II in the different S states (S_1, S_2, S_3, and S_0). The detailed fit parameters of the Mn EXAFS spectra are included in Table 1 and SI Tables 5 and 6.

to 100% $S_1Y_D^{ox}$. The S state composition of each sample was determined by EPR (SI Fig. 5 and SI Tables 3 and 4), and these data were used to generate the x-ray spectra of the pure S states.

X-ray Absorption Spectroscopy at the Mn K-Edge. Mn x-ray near-edge spectra (XANES) and EXAFS data were collected for all S state samples, ensuring the integrity of the samples and the absence of radiation damage to the structure of the Mn_4 core (Fig. 1). The resulting Mn spectra were similar to those from the same S states in Ca-containing PS II protein complexes isolated from spinach (28, 29) or the thermophilic cyanobacterium (18, 30). The edge shift that is apparent between the S_1 and S_2 spectra (Fig. 1*A*) indicates that Mn oxidation occurs during the S_1-to-S_2 transition. However, it is less clear that there is a shift between the S_2 and S_3 spectra, which suggests that Mn is not oxidized as the OEC proceeds from the S_2 to S_3 state (28). The edge position shifts to lower energy between the S_3 and S_0 spectra, as expected for $S_3 \rightarrow [S_4] \rightarrow S_0$ transition.

In the Fourier transform (FT) (Fig. 1*B*) of the Mn EXAFS data (SI Fig. 6), FT peak I is characteristic of the 1.8-Å Mn-oxo bridging ligand distances, FT peak II is best fit to two to three di-μ-oxo-bridged Mn–Mn interactions at ≈2.7 Å (Table 1), and FT peak III is from one mono-μ-oxo-bridged Mn–Mn and from Mn–Sr interactions. The presence of these three Fourier peaks is diagnostic for an intact bridged multinuclear Mn_4Ca(Sr) complex. The Mn_4Sr and Mn_4Ca clusters are essentially identical in terms of the structure of Mn_4-core; this is not surprising, because these clusters exhibit only small differences in their kinetic and spectroscopic properties.

Mn EXAFS of the S_1, S_2, and S_0 states are similar; however, as Fig. 1*B* shows, the S_3 state spectrum differs from those of the other S states. In the S_3 state the intensity of FT peak II decreases and peak III is significantly attenuated. This is best explained by changes in Mn–Mn and Mn–Sr distances and thus by structural changes in the OEC on the S_2 to S_3 and $S_3 \rightarrow [S_4] \rightarrow S_0$ transitions (Table 1 and SI Tables 5 and 6). The low intensity of FT peak III (there are 4 Mn/1 Sr) prevents reliable analysis of Mn–Sr interaction from the "Mn" point of view; however, as demonstrated below, the Sr EXAFS technique can clearly resolve the Sr–Mn interaction from the "Sr" point of view in all of the S states.

X-ray Absorption Spectroscopy at the Sr K-Edge. The Sr K-edge XANES of Sr-PS II, which corresponds to dipole-allowed transitions from the 1s core level to molecular orbitals with predominant p character, contains information about the valence and coordination environment of the absorbing atom. The Sr XANES spectra of Sr-PS II show that there is a pronounced difference between the S state spectra and the spectrum of *inactive* Sr-PS II after the Mn_4Sr cluster is disrupted by hydroxylamine (HYD) (Fig. 2*A*). This shows that in active PS II the Sr first coordination environment is different from that of free Sr^{2+} ion. Moreover, there are differences in the Sr XANES in the S_1, S_2, S_3, and S_0 states, indicating that Sr(Ca) is an integral part of the cluster. The Sr XANES is sensitive to changes in the electronic structure caused by changes in the oxidation state and geometry of the cluster as it cycles through the S states.

The structural changes of the S states are even more obvious in the Fourier transforms (FTs) (Fig. 2*B*) of the EXAFS spectra (SI Fig. 7) of Sr-PS II in the S_1, S_2, S_3, and S_0 states and the

Table 1. One- and two-shell simulations of Mn EXAFS Fourier peak II from the S_1, S_2, S_3, and S_0 states

Fit	Sample	Shell	*R*, Å	*N*	σ^2 (× 10^3), Å^2	Φ (× 10^3)	ε^2 (× 10^5)
			One shell				
1	S_1	Mn–Mn	2.73	1.1	1.7	0.20	0.10
2	S_2	Mn–Mn	2.74	1.1	1.6	0.22	0.10
3	S_3	Mn–Mn	2.76	1.4	3.3	0.31	0.15
4	S_0	Mn–Mn	2.73	1.3	2.0	0.30	0.16
			Two shells				
5	S_3	Mn–Mn	2.75	1.1	1.0*	0.23	0.11
		Mn–Mn	2.88	0.5	1.0*		
6	S_0	Mn–Mn	2.73	1.1	1.0*	0.28	0.14
		Mn–Mn	2.85	0.3	1.0*		

R is the Mn–Mn distance. S_0^2, an amplitude reduction factor (see *SI Text*, Eq. **1**), was set to 0.85. Range-extended EXAFS methodology can distinguish two Mn–Mn distances at ≈2.7 and ≈2.8 Å contributing to peak II in the S_1 and S_2 states (16, 17). Peak II in the S_1 and S_2 states can only be fit to one shell of Mn–Mn interactions at the resolution of conventional EXAFS. However, a two-shell fit is favored for the S_0 and S_3 states as indicated by an increased Debye–Waller factor for the one-shell fit. Φ and ε^2 are the goodness-of-fit parameters (see *SI Text*).
*Parameter was fixed.

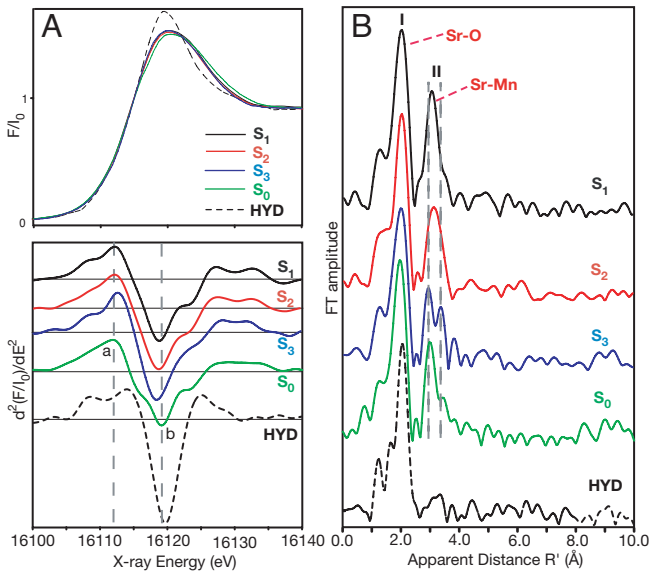

Fig. 2. Sr XAS of Sr-PS II from *T. elongatus*. (A) Sr K-edge XANES spectra (*Upper*) and the corresponding second derivatives of the XANES spectra (*Lower*) in the S_1, S_2, S_3, and S_0 states and an *inactive* control sample (HYD). The inflection point of the edges and the shape of the spectra are clearly different between the control and the intermediate S states. There are small but distinct differences in the S state spectra that are easier to see in the second derivatives (*Lower*). The two vertical dashed lines indicate the clear systematic differences in the Sr K-edge spectra between the S states; the feature labeled a shifts to higher energy and feature b shifts to lower energy as the OEC advances from S_0 through S_3 states. Other small differences are also seen in the second derivatives. (*B*) Fourier transforms of k^3-weighted Sr EXAFS (SI Fig. 7) in the different S states (S_1, S_2, S_3, and S_0), and an *inactive* control sample prepared by hydroxylamine treatment of Sr-PS II. The dominant Fourier peak I is due to ligating oxygens in the first coordination sphere to Sr. Peak II is best fit by four Sr–Mn interactions; two short distances at ≈3.5 and two longer Sr–Mn distances at ≈4.0 Å. FT peak II from Sr–Mn depends on the particular S state and shows that structure of cluster changes as the OEC advances through the S states, with a significant change occurring between the critical S_2-to-S_3 transition, suggesting that the cluster is flexible. The control sample shows only the FT peak from Sr–O backscattering, because the cluster is disrupted and the Sr–Mn interactions are lost. The detailed fit parameters of the Sr EXAFS spectra are included in Table 2 and SI Tables 7–9.

inactive control sample (HYD). The two major Fourier peaks, I and II, represent the radial distribution of the x-ray photoelectron backscattering from the atoms surrounding Sr. Fourier peak I is best simulated by one shell of seven to eight oxygen atoms at ≈2.5 Å (SI Table 7). Fourier peak II consists of at least two different Sr–Mn interactions at ≈3.5 Å and ≈4.0 Å in all S states (Table 2 and SI Tables 8 and 9). This Fourier peak is absent in the inactive control sample (HYD), because there are no Sr–Mn interactions in this sample. Relative to the S_1 state sample, FT peak II is broadened in S_2 and split in the S_3 and S_0 states; these changes are significant.

Discussion

Position of Sr Atom in the OEC in the S_1 State. Previously, the Ca EXAFS of the native PS II (14) and Sr EXAFS of Sr-reactivated PS II membranes (13) indicated proximity of the Ca at 3.4 Å and Sr at 3.5 Å to the Mn cluster in the S_1 dark-stable state of the OEC. The present study unambiguously demonstrates that Sr is proximate to the OEC in all S states and that significant changes occur in the Sr(Ca)–Mn interactions as the enzyme proceeds through the catalytic cycle, as seen in the FTs in Fig. 2*B* and Table 2. The Sr–Mn distances in the recently reported first synthetic heteronuclear Mn/Sr complex (31), where Mn and Sr are bridged by an oxo group, are similar to those observed in PS II. Therefore, it is likely that the Ca/Sr atom in PS II is bridged by a μ-oxo group to Mn atoms.

The best fits (Table 2) to the Sr EXAFS data (Fig. 2*B*) in the S_0 through S_3 states are obtained for Sr–Mn distances at ≈3.5 Å (short) and ≈4.0 Å (long). The best fits for the S_1 state are for 3:1, 2:2, and 2:1 short-to-long Sr–Mn ratio of vectors; however, the 3:1 fit is better than the others by 25–28% (Table 2 and SI Fig. 8). The best fit for the S_2 state is for a 3:1 or 2:2 short-to-long Sr–Mn ratio of vectors, with the fit for 2:2 being better by 21%. For the S_3 and S_0 states, a ratio of 2:2 provides the best fit (Table 2 and SI Fig. 8). This information is used below to model the position of Sr and the important changes in the short and long Sr–Mn distances during the S state transitions.

To model the position of the Sr atom in the S_1 state we combined information from the EXAFS fits (Table 2) and from polarized EXAFS measurements of Ca-containing PS II single crystals (18), from which three high-resolution Mn_4Ca structural models (I, II, and III) have been proposed (SI Fig. 9). For the three best fits (Table 2), there are three or two Sr–Mn vectors at ≈3.5 Å and one or two Sr-Mn vectors at ≈4.0 Å. For all three cases the Sr atom is displaced <1.2 Å from the position of Ca in the models, and is directly connected to the Mn core through a bridging oxygen atom. The Ca- and Sr-PS II are slightly different in their kinetic and spectroscopic properties (27), which may reflect differences in the interaction of Ca and Sr with the Mn atoms. Previous results from Ca EXAFS of plant PS II have shown that there are only two Mn–Ca distances (14) at <4 Å, compared with the four we have observed in Sr-PS II; it is possible that the two longer interactions are at >4 Å or were not discernible at the signal-to-noise ratio of the Ca EXAFS data (14). There is also evidence that Ca protects two of the four Mn atoms from reductants, suggesting a closer interaction between Ca and two of the four Mn atoms in the cluster (32). In Fig. 3*A* we use model II (from ref. 18) to illustrate the best possible position of the Sr atom (fit 1 in Table 2; 3:1 ratio) in the S_1 state. The experimental FT from the S_1 state of Sr-PS II is comparable with the FT calculated for the structure shown in Fig. 3*A*. Models I and III from Yano *et al.* (18) were also considered. The positions of Mn atoms in model III from Yano *et al.* (18) are identical to those in model II, resulting in the same Sr positions relative to the Mn_4 core (data not shown). The Sr/Ca atom in model III is ≈4 Å away from the μ_3-oxo-bridged oxygen, requiring μ-oxo bridges between Sr and Mn to explain the presence of short distances. Range-extended Mn EXAFS (17) results from oriented PS II membranes show that model I is less probable than models II or III.

Structural Changes in the OEC. Previous Mn EXAFS experiments demonstrated the absence of major changes in Mn–Mn distances of the Mn_4 core during the S_1-to-S_2 transition. Our present Mn and Sr EXAFS data (Figs. 1*B* and 2*B* and Tables 1 and 2) also show that there are no significant changes in the Mn–Mn and Sr–Mn distances during this transition. It is possible that the ratio of short:long Sr–Mn vectors changes from 3:1 (S_1) to 2:2 (S_2), on the basis of the quality of the fits (Table 2), indicating that one Sr–Mn distance changes from ≈3.5 to ≈4.0 Å during this transition. However, we cannot rule out the presence of the 2:2 ratio in the S_1 state or the 3:1 ratio in the S_2 state, because of the uncertainties in EXAFS fitting procedures.

A one-shell fit of peak II in the Mn EXAFS of the S_3 state (Table 1) shows an elongation of the Mn–Mn distance and an increased Debye–Waller factor compared with the S_1 and S_2 states. Introduction of the second Mn–Mn subshell improves the fit quality and resolves two distances (2.75 Å and 2.88 Å) among the di-μ-oxo-bridged Mn–Mn moieties. The low intensity of the Mn EXAFS FT peak III prevents reliable analysis of the changes in the mono-μ-oxo-bridged Mn–Mn and Mn–Sr interactions ≈3.2–3.5 Å.

Table 2. Two-shell simulations of Sr EXAFS Fourier peak II (Sr–Mn distances) from the S_1, S_2, S_3, and S_0 states

Fit	S state	Shell	*R*, Å	*N** (Sr–Mn interactions)	σ^2 ($\times 10^3$), Å^2	Φ ($\times 10^3$)	ε^2 ($\times 10^5$)
1	S_1	Sr–Mn	3.53	3	7.0	0.45	0.18
		Sr–Mn	4.02	1	7.0		
2	S_1	Sr–Mn	3.52	2	5.5	0.62	0.25
		Sr–Mn	3.99	2	5.5		
3	S_1	Sr–Mn	3.52	2	4.6	0.58	0.24
		Sr–Mn	3.99	1	4.6		
1	S_2	Sr–Mn	3.51	2	7.7	0.37	0.15
		Sr–Mn	3.97	2	7.7		
2	S_2	Sr–Mn	3.56	3	9.6	0.48	0.19
		Sr-Mn	4.03	1	9.6		
1	S_3	Sr-Mn	3.42	2	8.9	0.56	0.23
		Sr–Mn	3.94	2	8.9		
1	S_0	Sr–Mn	3.47	2	6.8	0.23	0.10
		Sr–Mn	3.98	2	6.8		

R is the distance between Sr and Mn. S_0^2, an amplitude reduction factor (see *SI Text*, Eq 1), was set to 1.0.
*The number of Sr–Mn interactions was fixed at integer values of 0, 1, 2, 3, and 4. σ is the Debye–Waller factor. Φ and ε^2 are the goodness-of-fit parameters. Details about parameters and fitting methodology are described in *SI Text* and SI Fig. 8.

The FT peak II in Sr EXAFS splits in the S_3 state (Fig. 2*B*) suggesting changes in Sr–Mn distances. The best fit (Table 2) for the S_3 state is for two short and two long Sr–Mn distances. The Sr–Mn interaction at ≈3.5 Å shortens to ≈3.4 Å, and the distance at ≈4.0 Å decreases to ≈3.9 Å during the S_2-to-S_3 transition. The fact that Mn–Sr interactions change during the S_2-to-S_3 transition is also in agreement with the different efficiency of Ca depletion in the S_3 state from that in other S states (33). Ca/Sr-depleted PS II cannot advance to the S_3 state; instead, a state designated $S_2Y_Z^{\bullet}$ is formed in which the Mn_4 core structure is close to that of the S_2 state and does not resemble the structure of the native S_3 state (12, 29). We propose that the single μ_3-oxygen of the Mn_4Ca structure is important for the formation of the S_3 state and that its properties are significantly altered in the absence of a coordinated Ca/Sr atom.

Completing the catalytic cycle in the S_3-to-S_0 transition, the di-μ-oxo-bridged Mn–Mn interactions exhibit shortening (Table 1) and recovery of peak III intensity in the Mn EXAFS (Fig. 1*B*). From Sr EXAFS, we can see that the Sr–Mn distances at 3.42 Å and at 3.94 Å increase to 3.47 Å and 3.98 Å, respectively. During the S_0-to-S_1 transition, the Sr–Mn distances increase further to ≈3.5 Å and ≈4.0 Å.

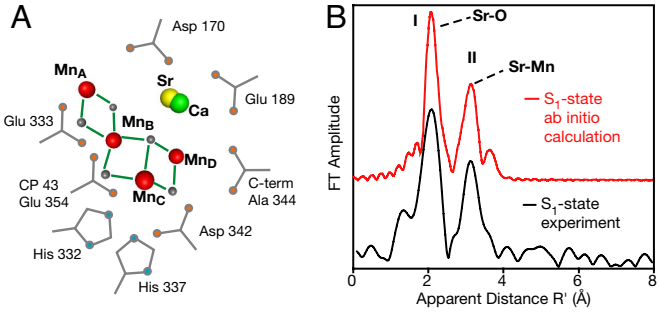

Fig. 3. (*A*) Ca atom (in green) and Sr atom (in yellow) were placed in the structural model derived from a polarized Mn EXAFS experiment on PS II single crystals (model II) (18) in the S_1 state. We note that the ligand/residues around the Mn_4Ca cluster in this model are putative. The number of the Sr–Mn vectors and the Sr–Mn distances are from the results of fits to Sr EXAFS data (fit 1 in Table 2); (Sr–$Mn_{B,C,D}$ at ≈3.5 Å and Sr–Mn_A at ≈4.0 Å). Only small changes in the Sr atom position are required, compared with the position of the Ca determined from polarized EXAFS studies of PS II crystals, to satisfy the Sr EXAFS data from Sr-PS II. (*B*) The Fourier transforms of the Sr EXAFS spectra from Sr-PS II of the S_1 state calculated by using the *ab initio* FEFF8 program for the placement of the Sr atom that is in accord with the best fit number 1 in Table 2. Coordinates of model II (18) with Sr as in fit 1 (Table 2) were used as input. *B* shows that peak II in the Sr EXAFS spectrum of PS II originates from Sr–Mn interaction. There is very good agreement between the experimental FTs from the Sr EXAFS spectra from Sr-PS II with the calculated FT for the model.

The generally accepted proton release pattern during the S_0-to-S_1, S_1-to-S_2, S_2-to-S_3, and S_3-to-S_0 transitions is 1, 0, 1, 2, respectively; although it has been reported that the proton release pattern is pH-dependent (34). EXAFS can provide only indirect information about protons, by the effect that protonations/deprotonations might have on the Mn–Mn/Sr(Ca) and Mn–O, N ligand atom distances. The shortening of one Mn–Mn distance observed during the S_0-to-S_1 transition is compatible with the deprotonation of an hydroxo (OH^-) bridge between Mn atoms to an oxo (O^{2-}) bridge (35, 36), and consistent with the release of one proton during this transition. During the S_1-to-S_2 transition there is no net release of protons and there are no significant changes in Mn–Mn/Ca distances. There is release of a proton during the S_2-to-S_3 transition, and the absence of any shortening in Mn–Mn distances allows us to speculate that the proton release proceeds differently for this transition. There are no EXAFS studies of S states between S_3 and S_0, when two protons are released. One speculation is that a proton is released from a hydroxo group that is a ligand of Ca/Mn (or from exogenous OH^-/H_2O) that is involved in the O–O bond formation, whereas another proton is released from a H_2O ligand of Ca/Mn (or from exogenous H_2O), which can be incorporated as a bridging OH^- ligand in the S_0 state. Ca, which can accommodate seven or eight ligands, is ideally suited for ferrying in H_2O/OH^- groups to the catalytic site.

Fig. 4 summarizes the structural changes accompanying the S_0 to S_3 catalytic cycle transition as deduced from Mn and Sr EXAFS. On the oxidation of one Mn atom, probably Mn_D (37, 38), during the S_1-to-S_2 transition, it is possible that the Sr atom moves away from one Mn (Mn_B, Mn_C, or Mn_D) leading to the change from 3:1 short:long Sr–Mn distances to a 2:2 ratio in the S_2 state. Alternatively, the 2:2 ratio can be present already in the S_1 state (lower fit quality; Table 1), thus remaining unchanged in the S_1-to-S_2 transition. During the S_2-to-S_3 transition, although the ratio of short-to-long vectors remains 2:2, there is a significant decrease in the Sr–Mn distances. From the Mn EXAFS the di-μ-oxo-bridged Mn–Mn distances increase during the S_2-to-S_3 transition; from ≈2.7–2.8 Å to ≈2.8–2.9 Å (Table 1). This result is similar to that detected by Mn EXAFS using PS II preparations from spinach (29). Future studies should aim at

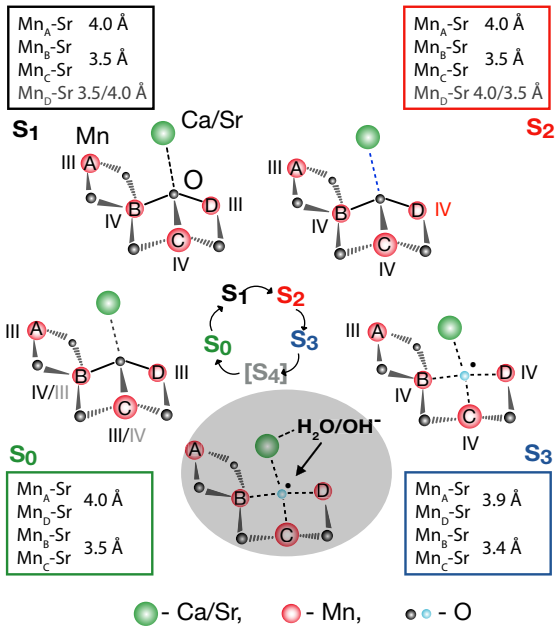

Fig. 4. Schematic of the structural changes accompanying the S state transitions in the $Mn_4Ca(Sr)$ cluster is placed within the context of the recent structural model II from single-crystal x-ray spectroscopy. The critical transition is the S_2-to-S_3 advancement, when the Mn–Mn di-μ-oxo bridge distances of the Mn_4 core become elongated from ≈2.7–2.8 Å to ≈2.8–2.9 Å. Simultaneously, Sr is drawn closer to the Mn core with the Sr–Mn interaction at ≈3.5 Å shortening to ≈3.4 Å and at ≈4.0 Å distance decreasing to 3.94 Å. We propose that this significant change is triggered by the ligand-centered oxidation of the oxygen atom that bridges the Mn with the Ca atoms. The Ca(Sr)–Mn distances in all of the S states are indicated in the boxes next to the S states. The critical bridging oxygen atom is shown in blue. The dashed line (blue) between Ca and the bridging atom in the S_2 state indicates the possible movement of Ca closer to two of the Mn atoms. The four dashed lines in the S_3 state indicate a change in the structure around the μ_3-oxo-bridged oxygen, probably from a tetrahedral to tetragonal distortion and leading to the changes in the Mn–Mn and Ca(Sr)–Mn distances. We note that a similar mechanism can be proposed by using model III (SI Fig. 9) from single-crystal EXAFS (18), that involves the oxidation of a different bridging oxygen atom during the S_2-to-S_3 transition.

identifying which particular Mn–Mn moiety in the model increases in distance.

Mechanism of Photosynthetic Water Oxidation. It is difficult to rationalize the changes in the Mn–Mn and Mn–Sr distances without significant involvement of the bridging O atoms. One hypothesis is that during the S_2-to-S_3 transition the oxidation occurs predominantly at a bridging oxygen ligand, triggering the structural changes in the OEC. An oxyl radical intermediate has been proposed on the basis of density functional theory (DFT) calculations (39, 40), including on a bridging position between two manganese atoms (41). Preliminary resonant inelastic x-ray scattering (RIXS) data show that the charge density change during the S_2-to-S_3 transition is much smaller than during the S_1-to-S_2 transition, supporting the hypothesis that the oxidation is predominantly ligand-centered.

We think that the observed structural changes in the S_2-to-S_3 transition are compatible with a primarily ligand-centered oxidation. The oxidized ligand in the S_3 state can interconvert between a bridging and a terminal ligand O atom (OH or H_2O) (42) resulting in an oxygen isotope exchange. Changes in Mn–O–Mn vibrational frequencies, the EPR properties (7, 27), rate of water exchange (43) on Ca to Sr substitution, and data presented here indicate that the critical oxygen atom is part of the Mn–O–Ca/Sr bridging structure.

Although, there are many proposed mechanisms for the photosynthetic water oxidation reaction that include variations on how the O–O bond is formed, there are two important favored mechanisms for water oxidation by the : (*i*) nucleophilic attack on Mn(V)=O or Mn(IV)-O$^\bullet$ by a metal (possibly Ca)-bound water molecule or hydroxide (9, 44); or (*ii*) reaction of a Mn-oxo unit with predominant radical character with an oxo/hydroxo/water ligand or an exogenous H_2O (29). Except for PS II there are few structurally defined catalysts competent to oxidize water at room temperature; Ru and Mn complexes provide examples (44, 45). A theoretical investigation of the Ru catalyst supported a Ru^{IV}-O$^\bullet$ moiety to promote the water-splitting reaction (46). Theoretical analysis of the OEC indicates that the formation of a low-lying ligand-oxygen radical precursor state may be required for forming the O–O bond (39). To reach this state, a structural rearrangement is needed at the S_2-to-S_3 transition. First, the changes in the Mn–Mn and Ca(Sr)–Mn distances require a model that involves a bridging oxygen atom (Fig. 4). This is probably the same oxygen where the oxidation occurs in the S_3 state, which triggers the formation of the O–O bond. We note, however, that the oxidation of a different bridging oxygen cannot be excluded. The bridging oxygen atom that is oxidized depends on whether we choose model II or III (18) for illustrating the general scheme of the mechanism. Second, the decrease in the Ca(Sr)–Mn distance during the S_2-to-S_3 transition favors the further formation of the O–O bond between a Ca-bound water or hydroxide and a Mn-bound oxygen. These two observations lead us to propose that the Ca-bound water or hydroxide and a critical oxo-bridging atom with predominantly radical character are the oxygen atoms involved in the formation of the all-important O–O bond in the water oxidation reaction.

Materials and Methods

Sample Preparation. Sr-containing PS II (Sr-PS II) was prepared as described in ref. 27, with the exception that the betaine concentration was decreased to 1 M. After elution from the Ni-affinity column, Sr-PS II was washed and concentrated by using centrifugal filtration devices (Ultrafree-15; Millipore). Sr-PS II was finally resuspended in 50% glycerol, 1 M betaine, 15 mM $CaCl_2$, 15 mM $MgCl_2$, 40 mM MES, pH 6.5 (adjusted with NaOH). Concentration of the Sr-PS II samples was ≈15 mg of Chl/ml.

EXAFS sample holders with inner dimension of 18 × 2.5 × 0.8 mm were filled with Sr-PS II samples. After dark adaptation for 1 h at room temperature, a freshly prepared stock solution (50 mM in ethanol) of phenyl-*p*-benzoquinone (PPBQ) was added to obtain a final concentration of 500 μM. PPBQ (Eastman Kodak) that was used in these experiments was recrystallized several times from ethanol. All of the flash illumination, EPR, and x-ray absorption measurements were performed directly on samples mounted in these holders. The samples were immediately frozen to 77 K in liquid nitrogen after flash laser illumination.

Metal Quantitation. Metal (Mn and Sr) quantitation was done by using a Perkin–Elmer 3110 Atomic Absorption Spectrometer equipped with an HGA 600 furnace. The quantitation yielded 37 ± 1 Chl/4 Mn and 1.0 ± 0.1 Sr/4 Mn.

Flash-Induced Illumination of PS II. A frequency-doubled (532 nm) Nd:YAG laser was used (8-ns pulsewidth) for flash illumination. To maintain maximal synchronization of the PS II centers on flash illumination, the fast recombination reaction between both the S_2 and S_3 states and the reduced form of the redox-active tyrosine residue Y_D must be suppressed. This was achieved by the application of one preflash, followed by a 60-min dark-adaptation period at room temperature. This procedure synchronizes the PS II centers into predominantly the $S_1Y_D^{ox}$ state. Each sample was then given zero, one, two, three, four, five, or six flashes at room temperature, with 1.5-s intervals between individual flashes. The light was focused on the sample by using cylindrical lenses. After the last flash, the samples were frozen immediately (within 1 s) in liquid nitrogen. The EPR spectra were collected, and the samples were stored at 77 K for further use in the XAS experiments. Alternatively, S_2 samples were prepared by 1-min continuous illumination at 200 K.

Control with Inactive Sr-PSII. The *inactive* Sr-PSII was prepared by adding 10 μl of a stock solution (100 mM) of hydroxylamine (NH_2OH) directly to the intact

Sr-PS II in the Lucite sample holder. After incubation for 20 min at room temperature in the dark, the sample was frozen in liquid nitrogen. NH_2OH-treated samples are indicated as HYD in the figures.

EPR Spectroscopy. Low-temperature X-band EPR spectra were recorded by using a Varian E109 EPR spectrometer equipped with a model 102 microwave bridge. For the multiline-signal measurements, the sample temperature was maintained at 8 K with use of an Air Products LTR liquid helium cryostat. Spectrometer conditions were as follows: microwave frequency, 9.21 GHz; field modulation amplitude, 32 G at 100 kHz; microwave power, 30 mW. EPR multiline-signal amplitudes were quantified by adding peak-to-trough amplitudes of four of the hyperfine lines upfield from g = 2, as indicated in SI Fig. 5*A*. For each sample, the four designated S_2 state multiline EPR signal peaks were quantified by using the amplitude of the Fe^{III} signal at g = 4.3 as an internal reference. The averaged results are shown as points in SI Fig. 5*B* normalized to the 1F value as 100%. The intensity of the multiline signal in the 1F samples and samples after continuous illumination were the same (within ± 10% uncertainty of the quantitative EPR technique), confirming the saturation of the sample with single laser flash illumination.

We used the Kok model as described in Messinger *et al.* (28) to calculate the S state population for each flash number and have compared the calculated S_2 state values (solid line, normalized to be 100% for 1F amplitude) to the normalized amplitudes (squares) shown in SI Fig. 5*B* (SI Tables 3 and 4). The error between the calculated and measured S_2 state populations was minimized. because of factors such as redox equilibrium between the cofactors in PS II, it is inevitable that some dephasing occurs while the OEC is advanced through the various S states. The original Kok model explains this by assuming two parameters: the miss probability (α) accounts for the percentage of centers that do not advance in each flash, and the double-hit probability (β) describes the percentage of centers that make two turnovers in a single flash. The value of β was first set to 0 based on the short pulsewidth of the Nd:YAG laser pulses. The possibility of double hits was considered in fit 2 and did not significantly improve the fit quality (SI Table 3). Oscillation characteristics obtained by more precise O_2 evolution measurements or with UV-absorption changes give comparable miss probability (27).

EXAFS Data Collection. X-ray absorption spectra were collected at the Stanford Synchrotron Radiation Laboratory (SSRL) on beamline 9-3 at electron energy 3.0 GeV and an average current 70–100 mA. The intensity of the incident x-rays was monitored by a N_2-filled ion chamber (I_0) in front of the sample. The radiation was monochromatized by a Si (220) double-crystal monochromator. To reduce the sample damage by x-radiation, the incident x-ray beam was defocused at the sample position. The total photon flux on the sample was limited to 1×10^7 photons per μm^2, which was determined to be nondamaging on the basis of detailed radiation-damage studies of PS II solution samples (30). The samples were protected from the beam during spectrometer movements between different energy positions by a shutter synchronized with the scan program. The samples were kept at 9 ± 1 K in a He atmosphere at ambient pressure by using an Oxford CF-1208 continuous-flow liquid He cryostat. Data were recorded as fluorescence excitation spectra by using a germanium 30-element energy-resolving detector (Canberra Electronics). For Mn XAS, energy was calibrated by the preedge peak of $KMnO_4$ (6,543.3 eV), which was placed between two N_2-filled ionization chambers (I_1 and I_2) after the sample.

Conditions for acquiring Sr EXAFS data on *T. elongatus* Sr-PS II samples closely resemble those for spinach solution and oriented samples and described in Cinco *et al.* (13, 15). The x-ray flux at 16–17 keV was 2.4×10^7 photons per μm^2 of sample. For energy calibration, we simultaneously measured the absorption spectrum of solid strontium acetate, whose edge peak was assigned the value 16,120.0 eV (15). Spectra were collected with 3-eV steps in the preedge region (15,970–16,070 eV), 1-eV steps from 16,070 to 16,134 eV, and 0.075-$Å^{-1}$ steps from $k = 2.0$–13.5 $Å^{-1}$. Sr EXAFS data were recorded during three x-ray beam times for S_1, S_2, and S_3 samples and during two beam times for S_0 samples. PS II samples from different preparations were used for each of these experiments. Identical spectra were obtained for all of these different PS II preparations.

ACKNOWLEDGMENTS. We thank M. Sugiura and A. W. Rutherford for continuing scientific discussions, D. Nocera and J. Messinger for ideas about the mechanism of water oxidation, and C. F. Yocum and G. C. Dismukes for discussions about the role of Ca. Synchrotron facilities were provided by the Stanford Synchrotron Radiation Laboratory (SSRL) operated by Department of Energy (DOE) Office of Basic Energy Sciences (OBES). The SSRL Biomedical Technology program is supported by the National Institutes of Health (NIH), the National Center for Research Resources, and the DOE Office of Biological and Environmental Research. This work was supported by NIH Grant GM 55302, and by the Director of the Office of Science, OBES, Division of Chemical Sciences, Geosciences, and Biosciences, DOE, under Contract DE-AC02-05CH11231.

1. Wydrzynski T, Satoh S (2005) *Photosystem II: The Light-Driven Water: Plastoquinone Oxidoreductase* (Springer, Dordrecht).
2. Peloquin JM, Britt RD (2001) *Biochim Biophys Acta* 1503:96–111.
3. Carrell TG, Tyryshkin AM, Dismukes GC (2002) *J Biol Inorg Chem* 7:2–22.
4. Hasegawa K, Ono TA, Inoue Y, Kusunoki M (1999) *Chem Phys Lett* 300:9–19.
5. Yachandra VK, Sauer K, Klein MP (1996) *Chem Rev* 96:2927–2950.
6. Sauer K, Yano J, Yachandra VK (2005) *Photosynth Res* 85:73–86.
7. Chu HA, Hillier W, Law NA, Babcock GT (2001) *Biochim Biophys Acta* 1503:69–82.
8. Debus RJ, Strickler MA, Walker LM, Hillier W (2005) *Biochemistry* 44:1367–1374.
9. Ferreira KN, Iverson TM, Maghlaoui K, Barber J, Iwata S (2004) *Science* 303:1831–1838.
10. Loll B, Kern J, Saenger W, Zouni A, Biesiadka J (2005) *Nature* 438:1040–1044.
11. Latimer MJ, *et al.* (1995) *Biochemistry* 34:10898–10909.
12. Latimer MJ, DeRose VJ, Yachandra VK, Sauer K, Klein MP (1998) *J Phys Chem B* 102:8257–8265.
13. Cinco RM, *et al.* (1998) *J Phys Chem B* 102:8248–8256.
14. Cinco RM, *et al.* (2002) *Biochemistry* 41:12928–12933.
15. Cinco RM, *et al.* (2004) *Biochemistry* 43:13271–13282.
16. Yano J, *et al.* (2005) *J Am Chem Soc* 127:14974–14975.
17. Pushkar Y, *et al.* (2006) *J Biol Chem* 282:7198–7208.
18. Yano J, *et al.* (2006) *Science* 314:821–825.
19. Boussac A, Rutherford AW (1988) *Biochemistry* 27:3476–3483.
20. Vrettos JS, Stone DA, Brudvig GW (2001) *Biochemistry* 40:7937–7945.
21. Westphal KL, Lydakis-Simantiris N, Cukier RI, Babcock GT (2000) *Biochemistry* 39:16220–16229.
22. Chu HA, Sackett H, Babcock GT (2000) *Biochemistry* 39:14371–14376.
23. Kimura Y, Hasegawa K, Ono T (2002) *Biochemistry* 41:5844–5853.
24. Kimura Y, Hasegawa K, Yamanari T, Ono TA (2005) *Photosynth Res* 84:245–250.
25. Strickler MA, Walker LM, Hillier W, Debus RJ (2005) *Biochemistry* 44:8571–8577.
26. Suzuki H, Taguchi Y, Sugiura M, Boussac A, Noguchi T (2006) *Biochemistry* 45:13454–13464.
27. Boussac A, *et al.* (2004) *J Biol Chem* 279:22809–22819.
28. Messinger J, *et al.* (2001) *J Am Chem Soc* 123:7804–7820.
29. Liang W, *et al.* (2000) *J Am Chem Soc* 122:3399–3412.
30. Yano J, *et al.* (2005) *Proc Natl Acad Sci USA* 102:12047–12052.
31. Mishra A, *et al.* (2007) *Chem Commun* 15:1538–1540.
32. Kuntzleman T, McCarrick R, Penner-Hahn J, Yocum C (2004) *Phys Chem Chem Phys* 6:4897–4904.
33. Boussac A, Rutherford AW (1988) *FEBS Lett* 236:432–436.
34. Rappaport F, Lavergne J (2001) *Biochim Biophys Acta* 1503:246–259.
35. Baldwin MJ, *et al.* (1994) *J Am Chem Soc* 116:11349–11356.
36. Robblee JH, *et al.* (2002) *J Am Chem Soc* 124:7459–7471.
37. Chu HA, Hillier W, Debus RJ (2004) *Biochemistry* 43:3152–3166.
38. Kimura Y, Mizusawa N, Yamanari T, Ishii A, Ono T (2005) *J Biol Chem* 280:2078–2083.
39. Siegbahn PEM, Crabtree RH (1999) *J Am Chem Soc* 121:117–127.
40. Lundberg M, Blomberg MRA, Siegbahn PEM (2004) *Inorg Chem* 43:264–274.
41. Siegbahn PEM (2000) *Inorg Chem* 39:2923–2935.
42. McEvoy JP, Brudvig GW (2006) *Chem Rev* 106:4455–4483.
43. Hendry G, Wydrzynski T (2003) *Biochemistry* 42:6209–6217.
44. Vrettos JS, Limburg J, Brudvig GW (2001) *Biochim Biophys Acta* 1503:229–245.
45. Yamada H, Siems WF, Koike T, Hurst JK (2004) *J Am Chem Soc* 126:9786–9795.
46. Yang X, Baik M-H (2006) *J Am Chem Soc* 128:7476–7485.